Ubiquity of shallow mesoscale circulations in the trades and their influence on moisture variance

Geet George[1,*], Bjorn Stevens[1], Sandrine Bony[2], Raphaela Vogel[2,3], and Ann Kristin Naumann[1,3]

[1]Max Planck Institute for Meteorology, Hamburg, Germany

[2]LMD/IPSL, Sorbonne University, CNRS, Paris, France

[3]Meteorological Institute, Universität Hamburg, Hamburg, Germany

[*]Corresponding author: Geet George, geet.george@mpimet.mpg.de

September 4, 2022

Abstract

Understanding drivers of cloud organization is crucial for accurately estimating clouds' feedback to a warming climate. Shallow mesoscale circulations are thought to play an important role in cloud organization, but they have not been observed. Here, we present observational evidence for shallow mesoscale overturning circulations (SMOCs) from divergence measurements made during the EUREC^{4}A field campaign in the north-Atlantic trades. Meteorological reanalyses reproduce the observed low-level divergence well and confirm SMOCs to be mesoscale features (ca. 200 km). Large mesoscale variability, five-fold the mean, is shown to be associated with the ubiquity of SMOCs. Furthermore, time-lag correlations suggest that SMOCs amplify mesoscale moisture variance at cloud-base and in the sub-cloud layer. Through their modulation of cloud-base moisture, SMOCs influence the drying efficiency of entrainment, thus yielding moist ascending branches and dry descending branches. The observed moisture variance differs from expectations from large-eddy simulations, which show largest variance near cloud top and negligible sub-cloud variance. The ubiquity of SMOCS and their coupling to moisture and cloud fields suggest that the strength and scale of mesoscale circulations are important in determining how clouds couple to climate, something which is not considered by present theories.

An understanding of the coupling between clouds and atmospheric circulation – one of the World Climate Research Programme's seven Grand Challenges – is a crucial missing link for constraining estimates of cloud feedback, i.e. the response of clouds to a warming climate [1, 2]. Cloud feedback estimates, especially those associated with low clouds, constitute one of the largest uncertainties in current assessments of climate sensitivity [3, 4]. The link between circulation and moisture variance at mesoscales ($\mathcal{O}$(100 km, 1 h)) influences the amount of clouds [5, 6] as well as their spatial organization [7]. Both aspects are crucial for low-cloud feedback [6, 8, 9]. Idealized large domain large-eddy simulations (LES) show that the spatial organization of clouds is coupled to shallow overturning circulations, which create moist and dry anomalies in their ascending and descending branches, respectively [10, 11, 12]. These circulations, while present in LES, are absent in the conceptual frameworks used to represent clouds in global climate models. This increases interest in determining if such circulations are evident in nature, and if so just how prevalent they are.

Recently, the field campaign EUREC^{4}A [*ElUcidating the RolE of Cloud-Circulation Coupling in ClimAte*; 13, 14] made extensive measurements of mesoscale horizontal divergence ($\mathcal{D}$), making it possible to explore the presence of such circulations and thus test inferences from modelling. The $\mathcal{D}$ measurements are samples averaged over a ∼220 km diameter circle for ∼1 h in the north-Atlantic trades [14, 15, 16], hereforth referred to as *circles* (Fig 1a,d). We analyze 65 circles from 11 flights spread over four weeks in January-February 2020. As shown in Fig. 1, a *flight-day* typically included two *circling-sets* (three consecutive circles) separated by an hour. Using EUREC^{4}A measurements we: (a) present observational evidence for shallow mesoscale overturning circulations (SMOCs hereafter), (b) characterize their spatial scales and frequency of occurence with help from meteorological reanalysis and (c) propose a mechanism by which SMOCs amplify moisture variance.

Evidence of SMOCs in EUREC^{4}A measurements

The time-mean $\mathcal{D}$ (Fig. 1b) is consistent with the theoretical understanding of the trades being on average a region of weak subsidence (ω) [17]. In the free troposphere, time-mean ω (∼24 hPa day^{-1}) as per the weak temperature gradient [WTG; 18] assumption, balances a mean cooling of ∼1.3 K day^{-1}, consistent with observed climatological cooling in the trades [19, 20]. $\mathcal{D}$ increases from the surface upwards and is then roughly constant through the bulk of the

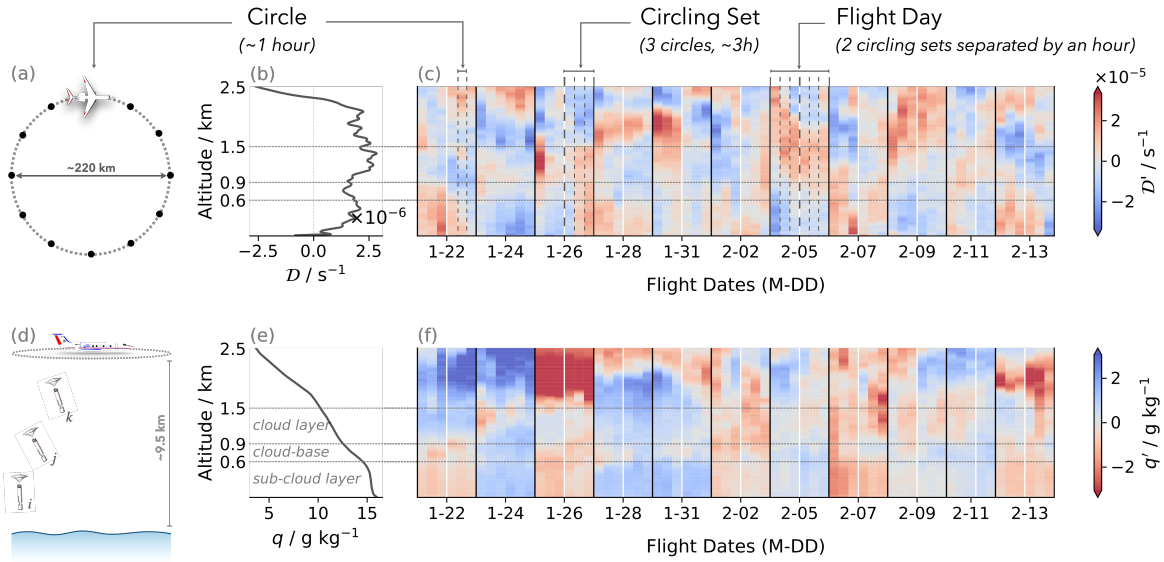

Figure 1: Divergence and humidity measurements from EUREC^{4}A | Vertical profiles of (b) divergence $\mathcal{D}$ and (e) specific humidity q averaged over EUREC^{4}A circles. Anomalies of $\mathcal{D}$ and q from time-mean ($\mathcal{D}'$ and q') are shown as hues in (c) and (f), respectively. Descriptions of terms explaining the sampling strategy (*circle, circling set* and *flight day*) are for typical samples. Deviations in some cases are detailed in [5] and [15]. The schematic on the left shows: (a) top-view of the HALO aircraft flying a circle with markers representing launch location of dropsondes and (d) a side-view depiction of multiple dropsondes (i, j, k) in flight.

trade-wind layer (0.3 - 2.3 km). This vertical coherence, however, is restricted to the time-mean and thus representative only of the larger synoptic scale.

At shorter timescales, $\mathcal{D}$ departs markedly from time-mean (Fig. 1c) indicating large vertical velocities unbalanced by radiation. The divergence anomaly ($\mathcal{D}'$) also changes sign between the sub-cloud and cloud layers. Averaged over circling-set and flight-day means (∼3 and ∼6-7 h, respectively), we find an anti-correlation between $\mathcal{D}'$ averaged over the sub-cloud ($\mathcal{D}'_{\mathrm{sc}}$) and cloud layer ($\mathcal{D}'_{\mathrm{c}}$) (Fig. 2a). Thus, when there is convergence in the sub-cloud layer, air diverges in the cloud layer and vice-versa. The prevalence of this $\mathcal{D}'$ dipole in the lower atmosphere indicates the presence of shallow overturning circulations, with circles sampling either ascending or descending branches. Given EUREC^{4}A's unbiased sampling and the sign changes in $\mathcal{D}$ over consecutive flights, we believe that the dipole is a mesoscale feature that is almost always apparent.

We investigate the vertical structure of these circulations, by analyzing composites of the lowest and highest quartiles of $\mathcal{D}_{\mathrm{sc}}$ (Figs. 3a-d). To distinguish the circulation features, analyses in Fig. 3 excludes data from 24.01.2020, the only day with flight-day mean missing the $\mathcal{D}'$ dipole (data-point in lower-left quadrant in Fig. 2a). Figs. 3a,b suggest that the circulations are shallow, being largely confined to the trade-wind layer (lower ∼2.3 km). The shallowness

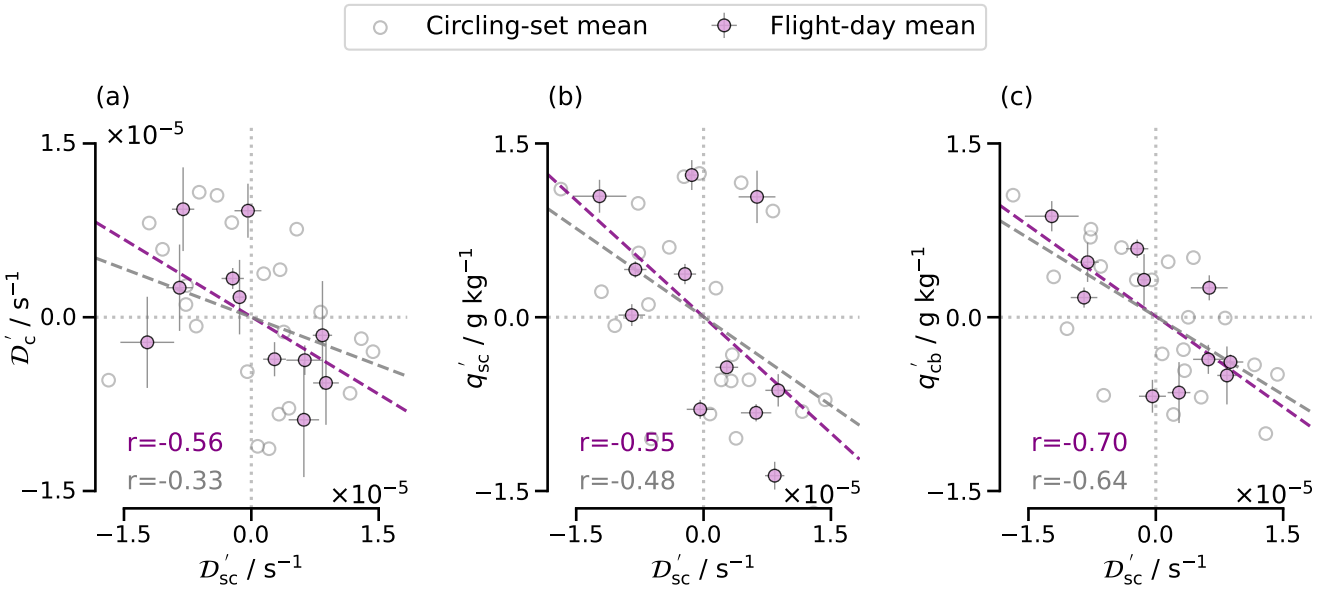

Figure 2: Relationships with sub-cloud layer divergence | Scatter plots against $\mathcal{D}'_{\mathrm{sc}}$ of (a) $\mathcal{D}'_{\mathrm{c}}$, (b) q'_{sc} and (c) q'_{cb} Subscripts 'sc', 'cb' and 'c' stand for averaging over sub-cloud (0-600 m), cloud-base (600-900 m) and cloud (900-1500 m) layers, respectively. Cross hairs show the standard deviation in the mean along altitude. r-values indicate Pearson's correlation coefficient for flight-day means (pink) and circling-set means (purple).

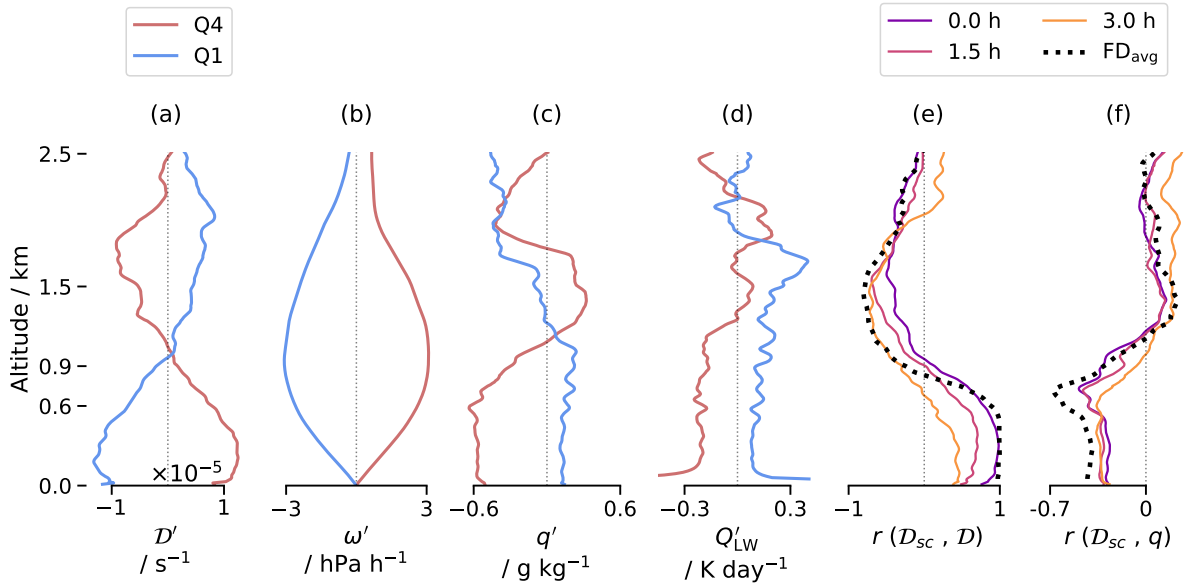

Figure 3: Quartile composites and correlations with sub-cloud divergence | Averaged profiles of anomalies of (a) $\mathcal{D}$ (b) subsidence ω, (c) q and (d) net longwave radiative cooling rate Q'_{LW} are shown for the lowest (Q1; strongest convergence) and highest (Q4; strongest divergence) quartiles of $\mathcal{D}_{\mathrm{sc}}$. Vertical profiles of Pearson's correlation coefficients (r-value) are shown between (e) $\mathcal{D}_{\mathrm{sc}}$ and $\mathcal{D}$ and (f) $\mathcal{D}_{\mathrm{sc}}$ and q. Dashed lines show correlation from flight-day averages ($\mathrm{FD}_{\mathrm{avg}}$), whereas the coloured profiles show correlation from circle-scale, but $\mathcal{D}$ lagging $\mathcal{D}_{\mathrm{sc}}$ in time as indicated in the legend. Profiles exclude circles from flight on 24.01.2020.

is made further evident by the fact that the strongest anti-correlation of $\mathcal{D}$ with $\mathcal{D}_{\mathrm{sc}}$ happens within and throughout the cloud layer (Fig. 3e). This shallowness is not unexpected given the large values of $\mathcal{D}'$ (Fig. 3a), which if maintained over a deeper layer would imply much larger ω'. Even for circulations as shallow as those observed, ω' goes up to 3 hPa hr^{-1} (Fig. 3b), which if sustained over a period of a day, would imply displacements of $\sim$670 m day^{-1}. If not compensated by adjacent branches of similar magnitude, such large displacements would lead to large pressure gradients and a deep saturated layer in the ascending branch, both of which are inconsistent with the shallow convective nature of the wintertime trades.

Ubiquity and spatial scale of SMOCs

To further test the idea that the circulations are mesoscale, we look into the European Centre for Medium-Range Weather Forecasts (ECMWF) reanalysis product [ERA5; 21] over a 10° x 10° domain, available at 0.25° spatial and 1 h temporal intervals. Reanalyses are thought to be reliable only for their synoptic reconstruction of divergence [e.g. 22, 23]. However, ERA5 turns out to reproduce mesoscale $\mathcal{D}$ from the EUREC^{4}A measurements in the lowest $\sim$2.5 km (see Fig. ED.1), and it does so independent of the assimilation of EUREC^{4}A soundings (see Methods). This ability of ERA5 to reproduce mesoscale $\mathcal{D}$ is likely due to the assimilation of scatterometer winds at the ocean surface and therefore presumably not limited to the EUREC^{4}A region and period.

ERA5's ability to capture $\mathcal{D}$ allows us to investigate SMOCs' occurence and spatial coverage. Similar to the measurements, we identify SMOCs in ERA5, by selecting grid points with a $\mathcal{D}'$ dipole. We then cluster such grid points into SMOC objects and fit them to equivalent ellipses (see Methods and Figs. 4a,b) to quantify their shape, size and orientation. Strikingly, SMOCs are present over the entire domain in Fig. 4a,b. We see a similar spatial prevalence of SMOCs for the entire EUREC^{4}A period: 58 $\pm$7% of the domain is covered by SMOCs (also see Fig. ED.3). The prevalence of the $\mathcal{D}'$ dipole in circles, combined with the spatio-temporal omnipresence of SMOCs in ERA5 shows that SMOCs are ubiquitous in the downstream trades.

Fig. 4c shows the distribution of the major and minor axes lengths and effective diameters (d_{eff}) of SMOC objects for the EUREC^{4}A period. The median values of all three lengths lie between 80 and 200 km, quantifying the size of these circulations' branches. This spatial scale derived from ERA5 fits well with the scale estimated from the measurements. The correlation of

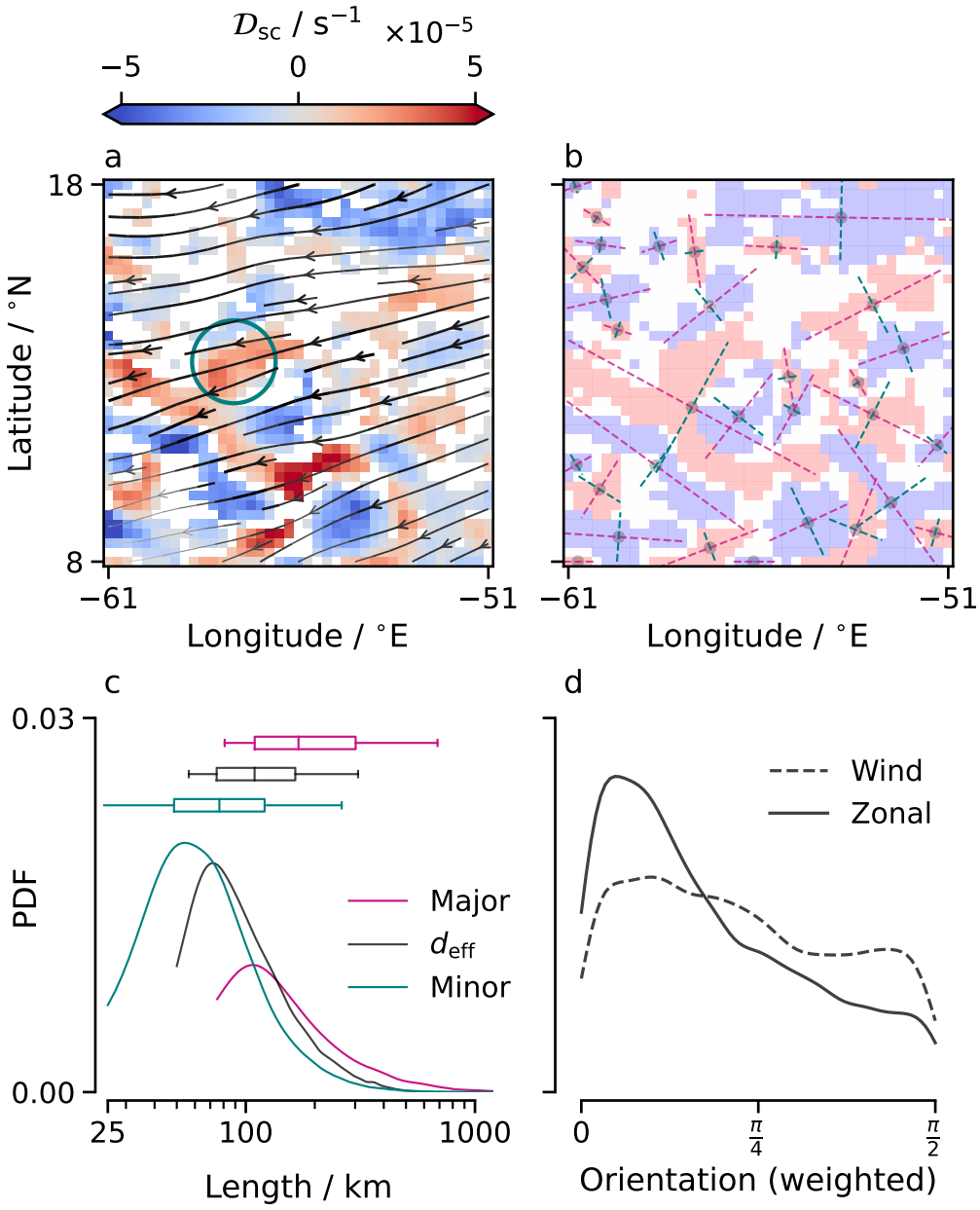

Figure 4: Scale and orientation of SMOC objects in reanalyses | (a) and (b) show a typical snapshot of ERA5 $\mathcal{D}'_{sc}$ for a 10° × 10° domain (2020-02-14 09:00 UTC). Overlaid streamlines in (a) show horizontal wind in the sub-cloud layer; thicker lines indicate stronger winds. The circle (teal) indicates the EUREC^{4}A circle. Similar $\mathcal{D}'_{sc}$ maps at 12 h snapshots for January-February, 2020 are shown in Fig. ED.3. Shading in (b) indicates convergent (blue) and divergent (red) clusters, with the centroid, major axis and minor axis, are shown for the SMOC objects (see Methods for details). (c) Gaussian-kernel probability density function (PDF; bin width ∼2 km) of major axis length (orange), minor axis length (green) and effective diameter (d_{eff}; black) for all SMOCs objects detected in the same domain every hour during the EUREC^{4}A period. Box-plots above show median (line in box), first and third quartiles (ends of box) and 5th and 95th percentiles (ends of whiskers). Lengths (in km) are derived with the approximation that 1° ≃ 100 km. (d) PDF (bin width $\pi/150$) of orientation of SMOC objects weighted by their area, with 0 indicating parallel and $\pi/2$ indicating tangential alignment of the major axis.

$\mathcal{D}$ with $\mathcal{D}_{sc}$ (Fig. 3e) shows that SMOCs persist for longer than 1 h, as the peak anti-correlation between $\mathcal{D}_c$ and $\mathcal{D}_{sc}$ occurs 2-3 hours apart, with $\mathcal{D}_c$ lagging $\mathcal{D}_{sc}$. Considering 9 m s^{-1} winds, airmasses would traverse the circle in ∼7 h (see Fig. 5) and flight-day measurements spanned ∼8 h. Hence, if SMOCs are of similar spatial scales as in Fig. 4c, one flight would sample only one branch of the circulation, which is consistent with what we observe, as $\mathcal{D}'_{sc}$ rarely changes signs through the course of a flight-day (Fig. 1c). These spatial scales, along with the adjacency of convergent and divergent cells, confirm that the dipole signals in measurements are indeed from circulations at the mesoscale.

Most SMOC objects are elongated rather than circular, as indicated by the offset between the major and minor axes length distributions in Fig. 4c. Fig. 4d shows that the elongation tends to align in the zonal direction, but there is little indication that SMOCs are concentrated along the direction of the near-surface (or cloud base) zonal wind.

Moisture variance and maintenance of SMOCs

SMOCs covary with the mesoscale moisture fields. Figs. 2b,c show that sub-cloud convergence is associated with moister sub-cloud and cloud-base layers. The converse is true for sub-cloud divergence. For flight-day averages, the strongest anti-correlation in the vertical occurs at 670 m (r=-0.67). To test whether SMOCS contribute to or are caused by such mesoscale variability, we investigate time-lag correlations between $\mathcal{D}_{sc}$ and specific humidity (q). The strongest anti-correlation occurs in the cloud-base layer at 0 h (Fig. 3f), whereas the strongest response of q_{sc} occurs 2-3 h later. The strengthening of the anti-correlation between $\mathcal{D}_{sc}$ and q_{sc} with time indicates the direction of causality, i.e. SMOCs amplify sub-cloud moisture variance.

Here, we develop a hypothesis of how SMOCs amplify the bottom-heavy moisture fluctuations (see bottom schematic in Fig. 5). In the rising branches, sub-cloud convergence increases the shallow-convective mass flux into the cloud-base layer [6, 24], which moistens cloud base. The moistened cloud-base reduces the drying efficiency of entrainment, a term representing small-scale mixing of dry air at cloud-base into the sub-cloud layer. Albright et al. [25] show that while entrainment is the dominant term balancing surface fluxes in the sub-cloud mass budget, the modulation of entrainment drying primarily results from moisture variability above the sub-cloud layer. Hence, with a moister cloud-base layer, the drying of the sub-cloud layer by entrainment becomes less efficient, thereby allowing surface moisture fluxes to accumulate

moisture in the layer. The argument applies conversely for the descending branch. This process would lead to an accumulation of moisture in the sub-cloud layer of the ascending branch, and a corresponding moisture deficit in the descending branch. This bottom heaviness is consistent with observations (Figs 3c and 3f).

Our hypothesis for the bottom-heavy moisture variance comes with two inferences. Firstly, the process is self limiting, as the moistening of the sub-cloud layer is proportional to its moisture deficit, which scales with cloud base height, thus potentially setting a limit to how large the moisture variance could be. Secondly, the time required for surface fluxes to respond to the change in entrainment drying efficiency means that SMOCs' moistening capacity has a time-dependence, i.e. the bottom heaviness is not an instantaneous response to SMOCs. This is consistent with the anti-correlations in Fig. 2b being stronger over flight-day means ($\sim$7-8 h) than over circling-set means ($\sim$3 h).

A maintenance of moist and dry branches in circulations will result in horizontal gradients of buoyancy and radiative cooling. Let's assume the lower and upper quartiles in q' and net longwave cooling, Q'_{LW} (Fig. 3c & d) represent the spatial differences between ascending and descending branches. The ascending branch (Q1) shows larger radiative cooling in the sub-cloud layer, which is opposite to what is expected from a circulation driven by radiative cooling differences [26]. Differences in shortwave heating between the composites are negligible (not shown). SMOCs are thus not driven by differential radiative cooling, at least during EUREC^{4}A. One potential driver for circulations though is the buoyancy gradient arising from the moisture difference [27]. Although the time-lag analysis suggests that buoyancy gradients do not trigger circulations, they likely amplify or maintain SMOCs. While studies suggest differences in both radiative cooling [26, 28, 29] and moisture-induced buoyancy [27, 29, 30] as possible causes for shallow circulations, at the scales observed in our data, it seems like the former inhibits SMOCs and the latter maintains or amplifies them.

A natural question then is how do SMOCs arise. Janssens et al. [12], based on minimal-physics large eddy simulations (LES), argue that they are triggered by shallow convection's intrinsic property to create unstable scale-growth in mesoscale moisture fields. Our findings of SMOCs being ubiquitous also in nature lends strength to their argument that SMOCs are indeed a signature of an intrinsic instability of the tropical atmosphere. However, in contrast to the bottom-heavy moisture variance associated with SMOCs in EUREC^{4}A data, LES show largest moisture variance near cloud-top and negligible variance in the sub-cloud layer [10, 11,

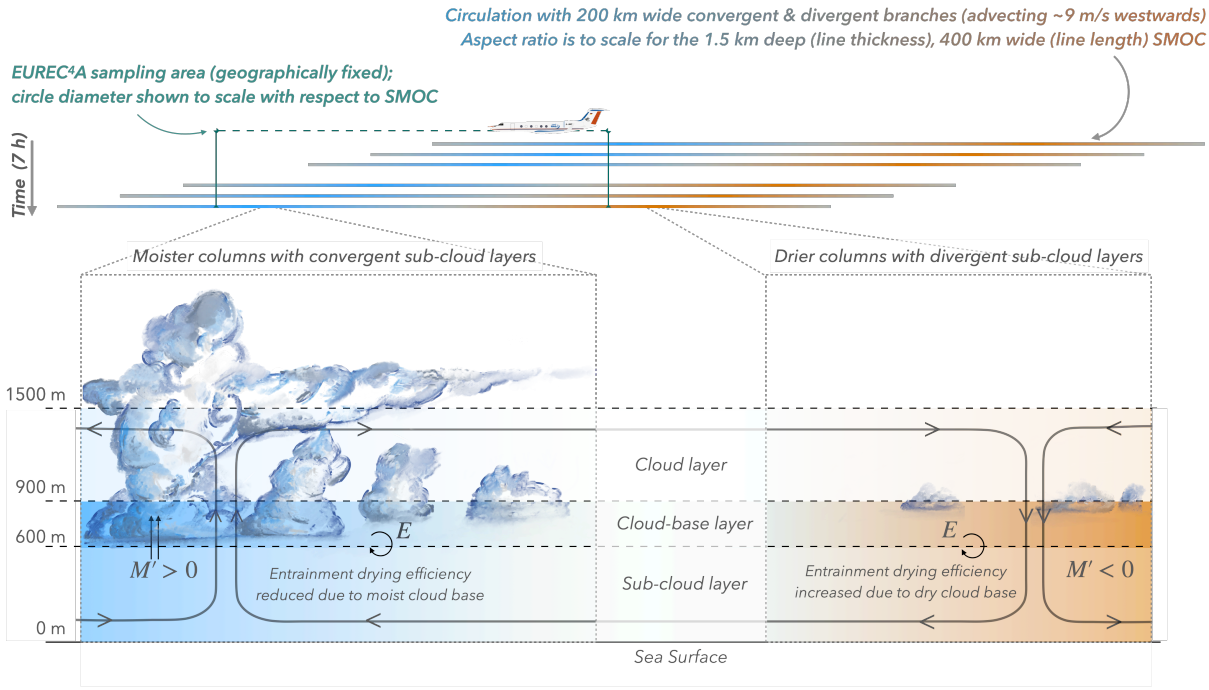

Figure 5: Schematic of our SMOCs hypothesis | E stands for entrainment rate and M' for shallow convective mass flux anomaly. The blue and brown hues represent moisture anomalies. The streamline shows the sense of the envisioned circulation. The aspect ratio of the advected SMOC at the top is shown to scale, underscoring the shallowness of the circulations. For depiction, it is assumed that conditions remain steady during the advection.

12]. In LES, the circulation-moisture interplay is shown to form a positive feedback, which is energized by latent heating anomalies in the cloud layer and their balance by the WTG adjustment. Although this mechanism explains the top-heavy variance, it is unclear whether such arguments would also be consistent with the bottom-heavy moisture variance associated with SMOCs in EUREC^{4}A data. While SMOCs may be triggered by condensation-driven heating anomalies, their strength and associated moisture variance may be modulated by factors such as precipitation [10, 31, 32], radiative cooling differences [26, 33] and sea-surface temperature gradients [34].

Conclusion

EUREC^{4}A measurements provide observational evidence for the prevalence of shallow mesoscale overturning circulations (SMOCs) in the trades and their influence on mesoscale moisture variance. Specifically:

- Measurements show an anti-correlation between divergence in the sub-cloud and cloud layers. We interpret this dipole as being indicative of shallow overturning circulations.

- The EUREC^{4}A measurements allow us to assess that the low-level divergence in ERA5 are representative of the measurements, even if the measurements are not being assimilated.

- With ERA5, we show that SMOCs are usually elongated features of ∼100-200 km and are ubiquituous (covering on average 58% of a 10° × 10° domain), thus explaining the large variability in mesoscale vertical velocity observed in the trades.

- Sub-cloud convergence is correlated with moister sub-cloud and cloud-base layers, indicating a bottom-heavy moisture variance. By affecting the efficiency of entrainment drying, SMOCs likely amplify moisture variance by extending the moisture fluctuations at cloud base down to the subcloud-layer.

- Convergent sub-cloud layers are 0.7 g/kg moister and radiate energy at rates that lead to 0.3 K/day larger longwave cooling rates than divergent sub-cloud layers, indicating that SMOCs are unlikely to be driven by radiative anomalies.

The ubiquity of SMOCS in EUREC^{4}A observations and their coupling to mesoscale moisture fluctuations [and cloudiness; 5, 6] indicate the mesoscale's control on how clouds couple to climate. The scale of the dominant energy in SMOCs is comparable to the grid scale of current climate models [∼100 km; 35], and if represented in these models, will likely be aliased to much larger scales. Therefore, exploring the instabilities and competing factors that drive SMOCs and the associated moisture fluctuations will improve our understanding of processes controlling cloud amount and organization. In this regard, differences between models and measurements (such as those in moisture variance) merit further investigation, something aided by our demonstration of the reanalyses' ability to represent such circulations. Such investigations are further motivated by Vogel et al. [6], who show with EUREC^{4}A observations that the variability in mesoscale vertical velocities, which we attribute to SMOCs, substantially controls variability of cloud amount in the trades.

Acknowledgments

The authors thank everyone who made the organization, collection and processing of EUREC^{4}A measurements possible. GG thanks Peter Blossey, Kerry Emanuel and Martin Janssens for insightful discussions and Hans Segura for his feedback on the manuscript. SB and RV were funded by the European Research Council EUREC^{4}A grant agreement 694768. AKN was funded by

the Deutsche Forschungsgemeinschaft (DFG, German Research Foundation) under Germany's Excellence Strategy – EXC 2037 'CLICCS - Climate, Climatic Change, and Society' – Project Number: 390683824. BS acknowledges support from H2020 funding (CONSTRAIN grant no 820829). HALO's operations during EUREC^{4}A were funded by the Max Planck Society (MPG), the German Research Foundation (DFG), the German Meteorological Weather Service (DWD) and the German Aerospace Center (DLR).

Code and Data Availability

The EUREC^{4}A circle measurements we used are from the JOANNE dataset v2.0.0 [16] and can be accessed with the DOI 10.25326/246. The radiative cooling profiles are from the dataset made available by Albright et al. [36] with the DOI 10.25326/78. The ERA5 data was accessed from Copernicus Climate Change Service (C3S) Climate Data Store (CDS) [37]. The data for the data-denial experiments performed with the IFS model used in this study are available with the following DOIs: 'ctrl' at 10.21957/4vgx-3f28 ; 'nd' at 10.21957/zfxz-3h02 and 'ndnr' at 10.21957/7zx9-6084 [38]. The code to make the plots in this manuscript and to perform the relevant analyses will be made available with a DOI.

References

[1] Sandrine Bony et al. "Clouds, circulation and climate sensitivity". In: *Nature Geoscience* 8.4 (Mar. 2015), pp. 261–268.

[2] Louise Nuijens and A Pier Siebesma. "Boundary layer clouds and convection over subtropical oceans in our current and in a warmer climate". In: *Current Climate Change Reports* 5.2 (2019), pp. 80–94.

[3] Gerald A. Meehl et al. "Context for interpreting equilibrium climate sensitivity and transient climate response from the CMIP6 Earth system models". In: *Science Advances* 6.26 (2020), eaba1981.

[4] Mark D. Zelinka et al. "Causes of higher climate sensitivity in CMIP6 models". In: *Geophysical Research Letters* (Jan. 2020).

[5] Geet George, Bjorn Stevens, Sandrine Bony, Marcus Klingebiel, and Raphaela Vogel. "Observed impact of meso-scale vertical motion on cloudiness". In: *Journal of the Atmospheric Sciences* (2021).

[6] Raphaela Vogel et al. *Strong cloud-circulation coupling explains weak trade cumulus feedback*. under review in Nature. 2022.

[7] Matthew D Lebsock, Tristan S L'Ecuyer, and Robert Pincus. "An observational view of relationships between moisture aggregation, cloud, and radiative heating profiles". In: *Shallow Clouds, Water Vapor, Circulation, and Climate Sensitivity*. Springer, 2017, pp. 65–82.

[8] Paulo Ceppi et al. "Cloud feedback mechanisms and their representation in global climate models". In: *Wiley Interdisciplinary Reviews: Climate Change* 8.4 (2017), e465.

[9] BE Mapes. "Gregarious convection and radiative feedbacks in idealized worlds". In: *Journal of Advances in Modeling Earth Systems* 8.2 (2016), pp. 1029–1033.

[10] Christopher S. Bretherton and Peter N. Blossey. "Understanding Mesoscale Aggregation of Shallow Cumulus Convection Using Large-Eddy Simulation". In: *Journal of Advances in Modeling Earth Systems* 9.8 (2017), pp. 2798–2821.

[11] Pornampai Narenpitak et al. "From Sugar to Flowers: A Transition of Shallow Cumulus Organization During ATOMIC". In: *Journal of Advances in Modeling Earth Systems* 13.10 (2021).

[12] M. Janssens et al. "Non-precipitating shallow cumulus convection is intrinsically unstable to length-scale growth". In: *Journal of the Atmospheric Sciences* (under review).

[13] Sandrine Bony et al. "EUREC4A: A field campaign to elucidate the couplings between clouds, convection and circulation". In: *Surveys in Geophysics* (Sept. 2017), pp. 1–40.

[14] B. Stevens et al. "EUREC^{4}A". In: *Earth System Science Data* 13.8 (2021), pp. 4067–4119.

[15] H. Konow et al. "EUREC^{4}A's *HALO*". In: *Earth System Science Data* 13.12 (2021), pp. 5545–5563.

[16] G. George et al. "JOANNE: Joint dropsonde Observations of the Atmosphere in tropical North atlaNtic meso-scale Environments". In: *Earth System Science Data* 13.11 (2021), pp. 5253–5272.

[17] Minghua Zhang et al. “The CGILS experimental design to investigate low cloud feedbacks in general circulation models by using single-column and large-eddy simulation models”. In: *Journal of Advances in Modeling Earth Systems* 4.4 (Apr. 2012).

[18] Adam H. Sobel, Johan Nilsson, and Lorenzo M. Polvani. “The Weak Temperature Gradient Approximation and Balanced Tropical Moisture Waves”. In: *Journal of the Atmospheric Sciences* 58.23 (2001), pp. 3650–3665.

[19] Dennis L. Hartmann and Kristin Larson. “An important constraint on tropical cloud - climate feedback”. In: *Geophysical Research Letters* 29.20 (2002), pp. 12-1-12–4.

[20] Sally A. McFarlane, James H. Mather, and Thomas P. Ackerman. “Analysis of tropical radiative heating profiles: A comparison of models and observations”. In: *Journal of Geophysical Research: Atmospheres* 112.D14 (2007).

[21] Hans Hersbach et al. “The ERA5 global reanalysis”. In: *Quarterly Journal of the Royal Meteorological Society* (June 2020).

[22] S. Bony et al. “On dynamic and thermodynamic components of cloud changes”. In: *Climate dynamics* 22.2-3 (Mar. 2004), pp. 71–86.

[23] Timothy A. Myers and Joel R. Norris. “Observational evidence that enhanced subsidence reduces subtropical marine boundary layer cloudiness”. In: *Journal of climate* 26.19 (Oct. 2013), pp. 7507–7524.

[24] Raphaela Vogel, Sandrine Bony, and Bjorn Stevens. “Estimating the Shallow Convective Mass Flux from the Subcloud-Layer Mass Budget”. In: *Journal of the Atmospheric Sciences* 77.5 (May 2020), pp. 1559–1574.

[25] Anna Lea Albright et al. “A new conceptual picture of the trade-wind transition layer”. In: *Journal of the Atmospheric Sciences* (submitted).

[26] Ann Kristin Naumann, Bjorn Stevens, and Cathy Hohenegger. “A moist conceptual model for the boundary layer structure and radiatively driven shallow circulations in the trades”. In: *Journal of the Atmospheric Sciences* 76.5 (May 2019), pp. 1289–1306.

[27] Da Yang. “Boundary Layer Height and Buoyancy Determine the Horizontal Scale of Convective Self-Aggregation”. In: *Journal of the Atmospheric Sciences* 75.2 (2018), pp. 469–478.

[28] Caroline Muller and Sandrine Bony. "What favors convective aggregation and why?" In: *Geophysical Research Letters* 42.13 (2015), pp. 5626–5634.

[29] Caroline Muller et al. "Spontaneous Aggregation of Convective Storms". In: *Annual Review of Fluid Mechanics* 54.1 (2022), pp. 133–157.

[30] Da Yang. "A shallow-water model for convective self-aggregation". In: *Journal of the Atmospheric Sciences* 78.2 (2021), pp. 571–582.

[31] A. Seifert and T. Heus. "Large-eddy simulation of organized precipitating trade wind cumulus clouds". In: *Atmospheric Chemistry and Physics* 13.11 (2013), pp. 5631–5645.

[32] T. J. Anurose et al. "Understanding the Moisture Variance in Precipitating Shallow Cumulus Convection". In: *Journal of Geophysical Research: Atmospheres* 125.1 (2020). e2019JD031178 10.1029/2019JD031178, e2019JD031178.

[33] Allison A. Wing and Kerry A. Emanuel. "Physical mechanisms controlling self-aggregation of convection in idealized numerical modeling simulations". In: *Journal of Advances in Modeling Earth Systems* 6.1 (2014), pp. 59–74.

[34] A. Foussard, G. Lapeyre, and R. Plougonven. "Response of Surface Wind Divergence to Mesoscale SST Anomalies under Different Wind Conditions". In: *Journal of the Atmospheric Sciences* 76.7 (2019), pp. 2065–2082.

[35] V. Balaji et al. "Requirements for a global data infrastructure in support of CMIP6". In: *Geoscientific Model Development* 11.9 (2018), pp. 3659–3680.

[36] A. L. Albright et al. "Atmospheric radiative profiles during EUREC^{4}A". In: *Earth System Science Data* 13.2 (2021), pp. 617–630.

[37] H Hersbach et al. "ERA5 hourly data on single levels from 1979 to present". In: *Copernicus Climate Change Service (C3S) Climate Data Store (CDS)* 10 (2018).

[38] A. C. M. Savazzi et al. "The representation of winds in the lower troposphere in ECMWF forecasts and reanalyses during the EUREC4A field campaign". In: *Atmospheric Chemistry and Physics Discussions* 2022 (2022), pp. 1–29.

[39] Sandrine Bony and Bjorn Stevens. "Measuring Area-Averaged Vertical Motions with Dropsondes". In: *Journal of the Atmospheric Sciences* 76.3 (Mar. 2019), pp. 767–783.

[40] Anna Lea Albright et al. "Observed subcloud layer moisture and heat budgets in the trades". In: *Journal of the Atmospheric Sciences* (2022).

[41] Geet George. "Observations of meso-scale cloudiness and its relationship with cloudiness in the tropics". PhD thesis. Staats-und Universitätsbibliothek Hamburg Carl von Ossietzky, 2021.

[42] Irina Sandu et al. *On the causes of systematic forecast biases in near-surface wind direction over the oceans*. Tech. rep. ECMWF Technical Memorandum, 2020.

[43] Christopher Lloyd. *Spatial data analysis: an introduction for GIS users*. Oxford university press, 2010.

[44] Stéfan van der Walt et al. "scikit-image: image processing in Python". In: *PeerJ* 2 (June 2014), e453.

Methods

EUREC^{4}A Dropsonde Measurements

The field campaign EUREC^{4}A took place in January-February, 2020 over the tropical north-Atlantic upwind of Barbados [see campaign overview in 14]. A core observation of EUREC^{4}A was area-averaged horizontal mass divergence and vertical velocity profiles derived from dropsonde measurements along the circumference of a circular flight path [39]. In EUREC^{4}A, the circular flight path was fixed to facilitate statistical sampling, with the centre at 57.67°W, 13.31°N and a diameter of 222.82 km (hereafter called EUREC^{4}A circles), and flown by the German High Altitude and Long range (HALO) aircraft. To keep the sampling consistent, here we exclude HALO's first (19.01.2020) and final (15.02.2020) research flights of the campaign and use data from 65 circles flown over the remaining 11 research flights, with a typical flight including 6 circles. Each circle typically launched 12 dropsondes spaced equally along the circumference over a period of an hour. On most flight days, HALO flew two sets of three circles each, called *circling sets*, with an excursion in between aimed at sampling upwind conditions. The two circling sets of a flight were carried out over a period of 7-8 hours; here termed as a *flight-day*. An overview of the circles flown during EUREC^{4}A and the dropsondes therein is provided in George et al. [16].

The dataset *Joint dropsonde Observations of the Atmosphere in tropical North atlaNtic mesoscale Environments*, with the backronym JOANNE [16], provides measurements from the EUREC^{4}A dropsondes. We use Level-4 data of JOANNE which provides the area-averaged quantities at 10 m vertical spacing from the circle measurements, such as horizontal mass diver-

353 gence ($\mathcal{D}$) and specific humidity (q). The measured quantities are from the surface up to 9.5 km,
354 which was the typical flight altitude during the circles. From the dataset provided by Albright
355 et al. [36], we use the net radiative cooling rates, with circle values obtained by averaging over
356 sondes in the circle.

357 Throughout the study, we use the terms *sub-cloud layer*, *cloud-base layer* and *cloud layer*
358 (referred to as 'sc', 'cb' and 'c' subscripts) to indicate altitude intervals of 0-600 m, 600-900 m
359 and 900-1500 m from the surface, respectively (also indicated in Fig. 1c). We define the cloud-
360 base layer as an extended transition layer between the sub-cloud and cloud layers to account for
361 thermodynamic variability that is most tightly coupled to that within the sub-cloud layer [40].
362 We explored, but found little benefit of trying to adapt these altitude intervals based on the
363 specific structure of the trade-wind layer for any given day [also see 41]. The symbol $'$ is also
364 used to indicate the anomaly from campaign mean. For example, $\mathcal{D}'_{\mathrm{sc}}$ is the divergence anomaly
365 from time-mean, averaged over the sub-cloud layer.

366 ERA5 divergence and comparison with EUREC^{4}A

367 We use $\mathcal{D}$ from ERA5 reanalysis products for time-period between 20-01-2020 00:00 UTC and
368 21-02-2020 00:00 UTC (parameter ID 155) available at 0.25° and 1 h intervals. First, we check
369 the reliability of ERA5 divergence, by comparing it with the circle observations. To make
370 a comparison collocated in space-time, we average ERA5 divergence spatially over grid-boxes
371 included within the standard-circle area for the hourly time-step nearest to the mean time of each
372 circle from observations. Figure ED.1 shows the agreement between these divergence profiles
373 from ERA5 and the corresponding ones from JOANNE averaged for every flight-day. Whereas
374 the profiles shown are averages over the flight-day, the estimate of r-values in the figure are from
375 values from all individual profiles in that day. Thus, the reanalysis' agreement of divergence with
376 observations is also at the circle time-scale (1 h) and not just when averaged over the flight-day
377 (6-7 h). The vertical structure of divergence simulated by ERA5 is the same as that seen in the
378 circle observations for most days, thus lending confidence in the use of reanalysis fields to study
379 the spatial and temporal variability in divergence.

380 The ERA5 products have assimilated information from the EUREC^{4}A dropsondes and ra-
381 diosondes. To check the influence of assimilation, we check the difference in divergence simulated
382 by data-denial experiments. These experiments are the same as those described by Savazzi et al.
383 [38], where a control simulation ('ctrl') similar to the ERA5 operational product is run along

with two data-denial experiments – one with no EUREC^{4}A dropsondes ('nd') and the other with no EUREC^{4}A dropsondes and radiosondes ('ndr') assimilated. We compare profiles between JOANNE and the experiments when the timestamps are within an hour of each other. The experiments have outputs available at 6 h intervals, and therefore, we only have 15 instances when $\mathcal{D}$ can be compared with JOANNE. Fig. ED.2 shows the square root of the mean squared error between $\mathcal{D}$ in the three experiments and $\mathcal{D}$ in JOANNE ($\mathrm{RMSE}_{\mathcal{D}}$). The assimilation results in very little improvement in the simulated fields of divergence. A similar conclusion was drawn by Savazzi et al. [38] for horizontal wind in the lowest 2 km. We believe that assimilation of near-surface horizontal winds from satellite-based scatterometers constrains the ERA5 near-surface divergence over ocean, making it possible to get an accurate vertical structure of D. The small impact of the soundings' assimilation of soundings is explained more generally by Sandu et al. [42] as "what often happens when one observing system is withdrawn from the data assimilation system is that other observing systems compensate for its loss and play a bigger role in constraining the analysis."

Segmenting SMOC objects

To detect SMOC objects in the ERA5 $\mathcal{D}_{\mathrm{sc}}$ field, we introduce a crude measure to detect which gridboxes can be included as being part of SMOCs objects. All gridboxes which have opposite signs of $\mathcal{D}'_{\mathrm{sc}}$ and $\mathcal{D}'_{\mathrm{c}}$ are considered SMOC cells (see Fig. 4a and Fig. ED.3). Such cells are further classified as either convergent cells if $\mathcal{D}'_{\mathrm{sc}} < 0$ or divergent if $\mathcal{D}'_{\mathrm{sc}} > 0$. Furthermore, the domain is segmented into multiple clusters of convergent and divergent cells based on a neighbor-identifying scheme where up to two orthogonal hops are made to consider a gridbox as a neighbor, or what is also known as a Queen's contiguity case in spatial autocorrelation analysis [43] (see Fig. 4b). We use the `label` function from the `measure` module of Python's `scikit-image` package (v0.19.2) [44] to perform this.

To get an estimation of the horizontal scale of these clusters, we estimate their major and minor axes, if they were fitted to an ellipse. Thus, the major and minor axes are defined as the larger and smaller second moments of area of these clusters, respectively. The first moment of area provides the coordinates for the centroids of clusters shown in Fig. 4b. The effective diameter (d_{eff}) of the clusters is the diameter of a circle equivalent in area to the area of the cluster. To avoid irregularities due to the coarse-resolution of the ERA5 domain, we only consider clusters with major axis length greater than 0.75° as SMOC objects.

Extended Data

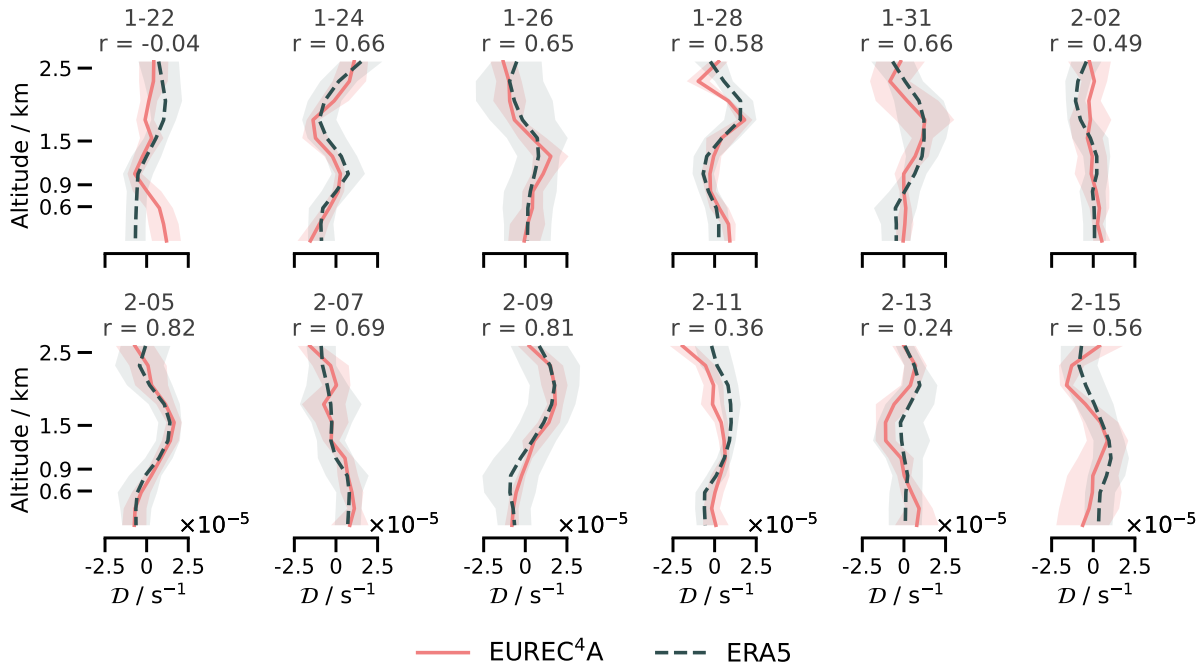

Figure ED.1: Profiles of flight-day mean divergence from EUREC^{4}A dropsonde measurements (JOANNE; red solid line) shown with the interquartile range (red shaded). Corresponding profiles from ERA5 by averaging over gridboxes within the circle, with time-steps nearest to the ones included in the JOANNE flight-day mean (grey dotted line) and the interquartile range (grey shaded) therein are overlaid. Above each profile, the flight date is given along with the correlation r-value between JOANNE and ERA5 profiles for all circles on that flight-day.

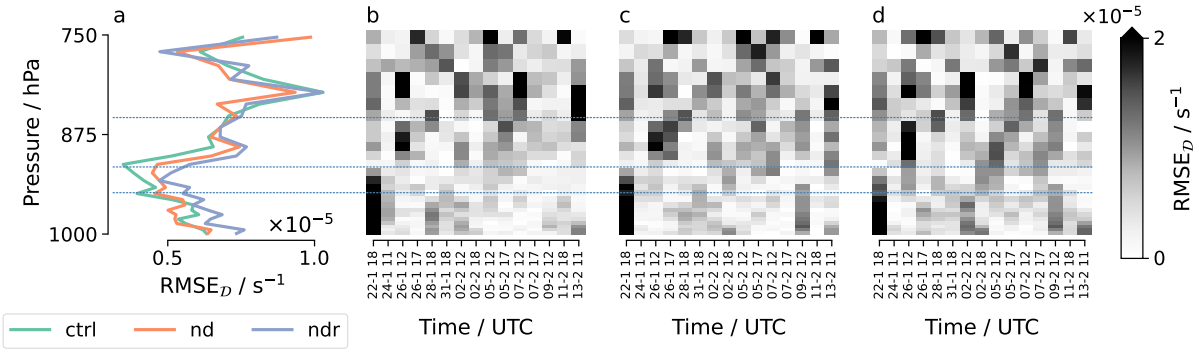

Figure ED.2: (a) Vertical profiles of RMSE$_\mathcal{D}$ for the control and two data-denial experiments. Hues show RMSE$_\mathcal{D}$ for experiments (b) 'ctrl', (c) 'nd' and (d) 'ndnr' at all instances where timestamps in the experiments are within an hour of available circle measurements from JOANNE. The tick labels on the X-axis are in the format 'DD-M H', where D, M and H stand for date, month and hour, respectively. The overlaid horizontal lines (dotted blue) indicate, from top to bottom, the tops of the sub-cloud layer, cloud-base layer and cloud layer.

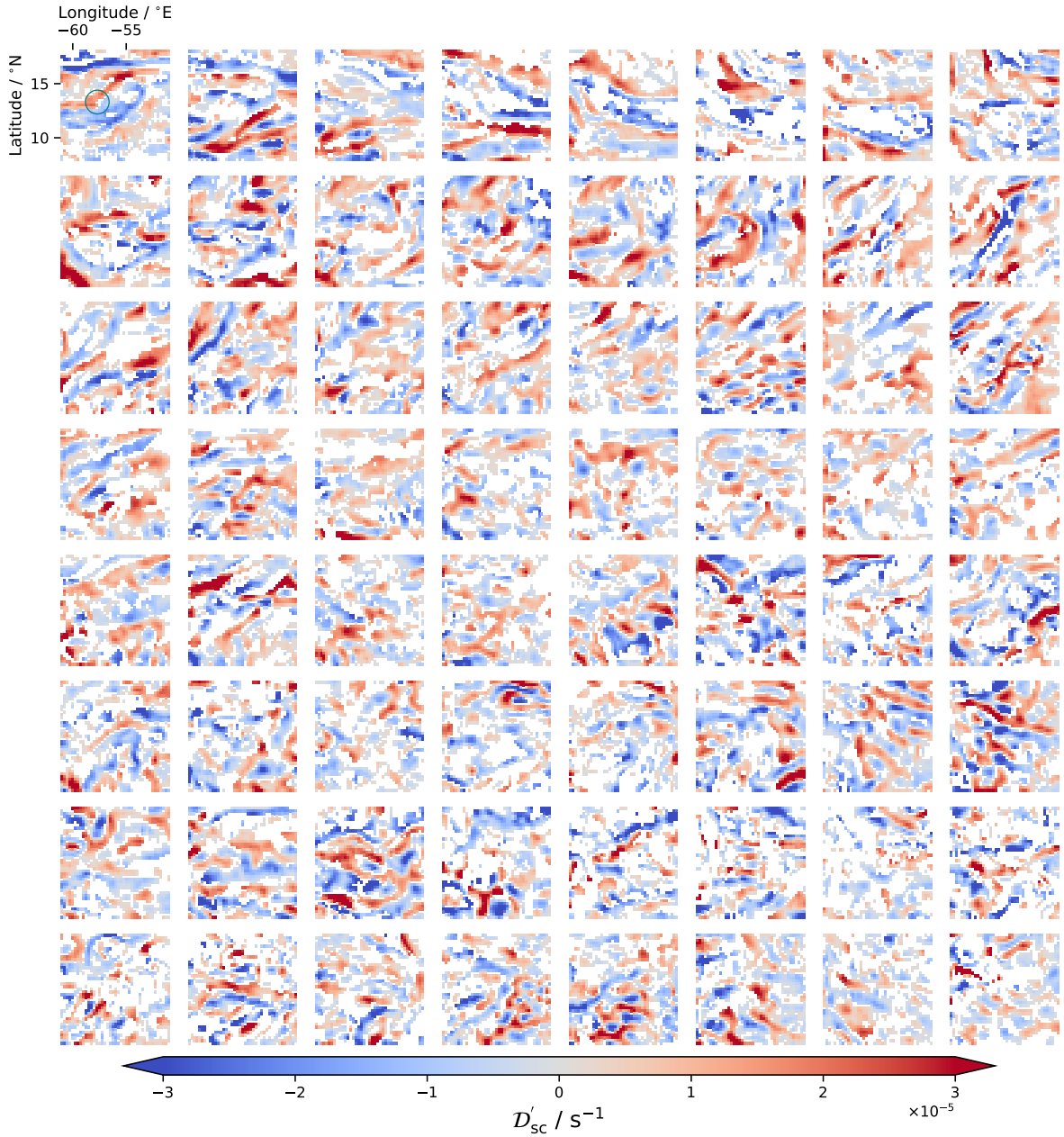

Figure ED.3: Spatio-temporal ubiquity of SMOCs in the trades shown by ERA5 $\mathcal{D}'_{sc}$ plotted over a 10°× 10° domain for the EUREC^{4}A period at every 12 h timestep. Only gridboxes which have opposite signs of divergence anomaly in the sub-cloud and cloud layer are shaded, reds showing converging airmasses in the sub-cloud layer and blue diverging. Unshaded gridboxes (in white) are where sub-cloud and cloud layers have same sign of $\mathcal{D}'$. The first box shows the spatial scale of the domain along with a circle (teal) showing scale of EUREC^{4}A measurements.